Computational Materials Science 256 (2025) 113954

Contents lists available at ScienceDirect

Computational Materials Science

journal homepage: www.elsevier.com/locate/commatsci

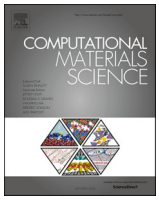

Full Length Article

Unraveling the effects of multi-phonon scattering mechanisms on lattice thermal conductivity of $La_2Zr_2O_7$, $La_2Sr_2AlO_7$ and $LaPO_4$ prototype thermal barrier coatings from both perturbative and non-perturbative methods based on machine learning potential

Huaxuan He [a], Xingming Wang [a], Yuzhou Hao [b], Chao Zeng [a], Jianyu Li [c], Haoliang Liu [a], Zhibin Gao [b,*], Jing Feng [c,*], Bing Xiao [a,*]

[a] State Key Laboratory of Electrical Insulation and Power Equipment, School of Electrical Engineering, Xi'an Jiaotong University, Xi'an Shaanxi 710049, China
[b] State Key Laboratory for Mechanical Behavior of Materials, School of Materials Science and Engineering, Xi'an Jiaotong University, Xi'an 710049, China
[c] Faculty of Materials Science and Engineering, Kunming University of Science and Technology, Kunming, Yunnan 650093, China

ARTICLE INFO

Keywords:
Thermal barrier coatings
Three- and four-phonon scatterings
Linear Boltzmann transport equation
Kubo-Green formula
Phonon quasi-particle spectrum

ABSTRACT

The multi-phonon scattering mechanisms and lattice thermal conductivity of the three prototypes thermal barrier coatings including the $La_2Zr_2O_7$, $La_2SrAl_2O_7$ and $LaPO_4$ are studied using both the perturbative linear Boltzmann transport equation (LBTE) under the three- and four-phonon scattering schemes and the non-perturbative equilibrium molecular dynamics simulations coupled with Kubo-Green formula (EMD-KG) method based on properly trained and validated moment tensor potentials (MTPs). It is revealed that incorporating multi-phonon scatterings in LBTE method under either 3ph or 3ph + 4ph schemes could underestimate the lattice thermal conductivity of the thermal barrier coatings mainly due to the poor description of heat conduction for highly localized phonon modes (locons) in the temperature renormalized phonon spectrum within the perturbative approach. Meanwhile, the non-perturbative EMD-KG method not only could accurately reproduce the values of lattice thermal conductivity that are in good agreement with experiments in the temperature range between 300 K and 1500 K, but also correctly predicts the flat thermal conductivity at elevated temperatures for all three thermal barrier coatings. The phonon quasi-particle spectrum and quasi-particle lifetimes are also obtained, and results elucidate that the perturbative LBTE method predicts the phonon relaxation times significantly smaller than those of phonon quasi-particle lifetimes calculated from non-perturbative EMD method especially for the low-frequency phonon modes. Therefore, the EMD-KG method combined with highly accurate machine learning potential provides a numerically efficient and physically sound methodology to study phonon transport properties of thermal barrier coatings.

1. Introduction

Thermal barrier coatings (TBCs) play a critical role in protecting components from thermal damage and maintaining temperature stability, and which are not only indispensable in civilian applications such as automobiles [1–3] and cables [4], but also widely used in cutting-edge fields, including nuclear power plants [5], large gas turbines [6], and aerospace vehicles [7]. Currently, the most widely used thermal barrier coating material is yttria-stabilized zirconia (YSZ). However, YSZ undergoes phase transitions at temperatures above 1200 °C, leading to the formation of cracks and eventual failure of the coating [8]. Therefore, to meet the demands of higher temperature applications, it is necessary to explore thermal barrier coating materials with better stability and lower thermal conductivity. In the past several decades, three promising rare-earth-based materials, namely pyrochlore ($Ln_2Zr_2O_7$), double perovskite ($Ln_2SrAl_2O_7$), and monazite structures ($LnPO_4$) have attracted great attentions world widely as probable replacements for YSZ, where Ln refers to the rare earth metals including La, Gd, Sm. In recent years, the high entropy alloying strategy was successfully demonstrated to prepare multi-component solid solutions of pyrochlore and monazite structures with strong cation disordering at Ln lattice sites, leading to the further reduction of overall lattice thermal conductivity,

* Corresponding authors.
E-mail addresses: zhibin.gao@xjtu.edu.cn (Z. Gao), jingfeng@kust.edu.cn (J. Feng), bingxiao84@xjtu.edu.cn (B. Xiao).

https://doi.org/10.1016/j.commatsci.2025.113954
Received 4 April 2025; Received in revised form 27 April 2025; Accepted 28 April 2025
Available online 5 May 2025

compared to those of fully ordered lattice structures [9–11].

As insulators, the thermal conductivity of those prototype structures ($Ln_2Zr_2O_7$, $Ln_2Sr_2AlO_7$ and $LnPO_4$) is primarily determined by lattice thermal conductivity, which arises from lattice vibrations. Compared to conventional crystalline materials, the lattice thermal conductivity of thermal barrier coatings even within a fully ordered lattice structure is quite low, i.e., 1 $W{\cdot}m^{-1}{\cdot}K^{-1}$–3 $W{\cdot}m^{-1}{\cdot}K^{-1}$. Such low intrinsic lattice thermal conductivity may arise from the different phonon scattering mechanisms such as point defects (O vacancies particularly), isotopes, grain boundary and most importantly the phonon–phonon interactions, as suggested in many previous experimental and theoretical studies [12–14]. Nevertheless, the phonon mean free path of crystalline thermal barrier coatings was revealed to approach the Ioffe-Regel limit even at the moderate temperature (~1000 K), indicating the multi-phonon scattering processes could dominate the intrinsic lattice thermal conductivity of them even at the room temperature regardless of the presence of defects and grain boundary [15,16]. Furthermore, the transportation behaviors of highly localized phonons could not be reliably described as extended lattice waves due to their extremely short mean free path and low atomic participation ratio in the vibration patterns [17]. Some interesting concepts for describing the phonon modes such as propagons, diffusons and locons that are originally invoked for amorphous materials were adopted to clarify different phonon transportation channels in thermal insulating materials [17,18]. Therefore, understanding the multi-phonon scattering mechanisms in lattice structures of thermal barrier coatings is critical not only in terms of optimizing the thermal insulation performance but also vital for unraveling the role of higher order phonon–phonon interactions that go beyond the normal three-phonon scattering process in those thermal insulating materials.

Recent advances in the phonon transportation theory and computational tools allow the direct calculations of the second, third and even fourth order of interatomic force constants for crystalline materials, enabling the investigation of three- and four-phonon scattering processes and their impacts on the lattice thermal conductivity of thermal insulating materials under the perturbative linear Boltzmann transport equation (LBTE) [19,20]. However, the number of symmetrically reduced inter-atomic force constants typically increases drastically with the total number of atoms (N) within the modelling crystal structures, i.e., 27 N^3 and 81 N^4 for third and fourth order force constants, respectively [21]. The overall computational costs for obtaining the higher order force constants and for solving the LBTE are expected to be quite significant for most thermal barrier coatings having relatively complex crystal structures such as pyrochlore ($Ln_2Zr_2O_7$). Additionally, the conventional methodology and workflow for evaluating the lattice thermal conductivity in crystalline materials are obviously no appliable to the high-entropy thermal barrier coatings due to the occupation disordering in the lattice structures. To counteract those challenges in calculating lattice thermal conductivity for large complex lattice structures, the computational workflow based on highly accurate machine learning potentials that are trained from the first-principles calculation datasets has been developed to interface with either the perturbative LBTE method or the non-perturbative molecular dynamics simulations (equilibrium and non-equilibrium), allowing the fast accessing of multi-phonon interactions and lattice thermal conductivity for both crystalline and amorphous structures in principle [22–25]. Compared to that of LBTE method, the use of molecular dynamics simulations also shows an obvious advantage that all higher order lattice anharmonic effects can be included in calculating the lattice thermal conductivity from the Kubo-Green formula and the phonon spectral energy density (pSED) [20]. Regarding the use of such a methodology to predict the lattice thermal conductivity for thermal barrier coatings, two recent works are mentioned here. Luo et al. trained the moment tensor potential (MTP) for the pyrochlore $La_2Zr_2O_7$ structures and further conducted a dual-channel analysis of phonon transport mechanism in $La_2Zr_2O_7$, proposing an explanation for the slower decline in thermal conductivity of the structure at high temperatures based on phonon diffusion behavior of optical modes [16]. Meanwhile, Simoncelli and coworkers conducted the theoretical analysis on the phonon transportation behaviors of pyrochlore-$La_2Zr_2O_7$ and monizate-$LaPO_4$ using the respective machine learning potentials in combination with LBTE and Wigner formula for different phonon channels, i.e., propagons and diffusons [26,27]. Those studies clearly demonstrated the rather complicated lattice anharmonicity and distinct phonon conduction channels in thermal insulating materials. Nevertheless, a comprehensive comparison study of multi-phonon scattering mechanisms (three-phonon, four-phonon and all higher order phonon interactions) among the three representative prototype thermal barrier coatings including pyrochlore-$La_2Zr_2O_7$, double-perovskite-$La_2Sr_2AlO_7$ and monazite-$LaPO_4$ has not been reported before in the literatures using the methodology based on machine learning potentials. Otherwise, the reliability of using equilibrium molecular dynamics simulation based on machine learning potential and the Kubo-Green formula to predict the lattice thermal conductivity of complex crystal structures with either the low symmetry or a large unit cell was not thoroughly addressed in all previous theoretical studies especially in comparison to that of either LBTE method containing 3 and 4 phonon scatterings or experimental results. Finally, the use of phonon spectral energy density (pSED) to elucidate the impacts of all higher order phonon interactions on the phonon quasi-particle lifetimes and lattice thermal conductivity was probably overlooked in previous studies for thermal barrier coatings.

In this paper, we successfully developed and thoroughly tested a universal workflow for efficiently and reliably predicting and analyzing the phonon transport properties of three prototype crystal structures (pyrochlore-$La_2Zr_2O_7$, double-perovskite-$La_2SrAl_2O_7$ and monazite-$LaPO_4$) as thermal barrier coatings using the machine leaning potentials in combination with perturbative LBTE method and non-perturbative equilibrium molecular dynamics simulations. Our current work particularly focused on impacts of higher order phonon scattering mechanism including the third order, the fourth order and all orders on the phonon quasi-particle lifetimes and lattice thermal conductivity of crystalline thermal barrier coatings using Kubo-Green formula and pSED from large-scale molecular dynamics simulations at different temperatures. The results clearly revealed the significance of the incorporation of all higher order phonon interactions in accurately predicting the lattice thermal conductivity of thermal barrier coatings using molecular dynamics simulations, in comparison to the strong suppressing of phonon heat conduction at high temperature using LBTE method after considering both 3- and 4-phonon scatterings, providing the freshly new physics insights on the controversial role of multi-phonon scattering processes in the lattice thermal conductivity.

2. Computational methods and details

2.1. Overview of the workflow

Here, we briefly review the proposed workflow for accessing the lattice thermal conductivity and multi-phonon scattering mechanisms using the molecular dynamics simulations and lattice dynamic calculations based on machine learning potentials trained from first-principles calculations. The overall workflow is illustrated in Fig. 1, including three different stages in the whole procedure. In the first stage, the first-principles molecular dynamics simulations are conducted for three prototype thermal barrier coatings (pyrochlore-$La_2Zr_2O_7$, double-perovskite-$La_2Sr_2AlO_7$ and monazite-$LaPO_4$) under either the constant temperature (canonical ensemble) or the fixed temperature range to generate the training and validation datasets for the subsequent machine learning potential training process. The machine learning potential employed in this work is known as the moment tensor potential (MTP) which uses atomic configurations, total energies, interatomic forces and stress tensors as the input data for the training [28,29]. The training and validation of the MTPs for the three crystal structures

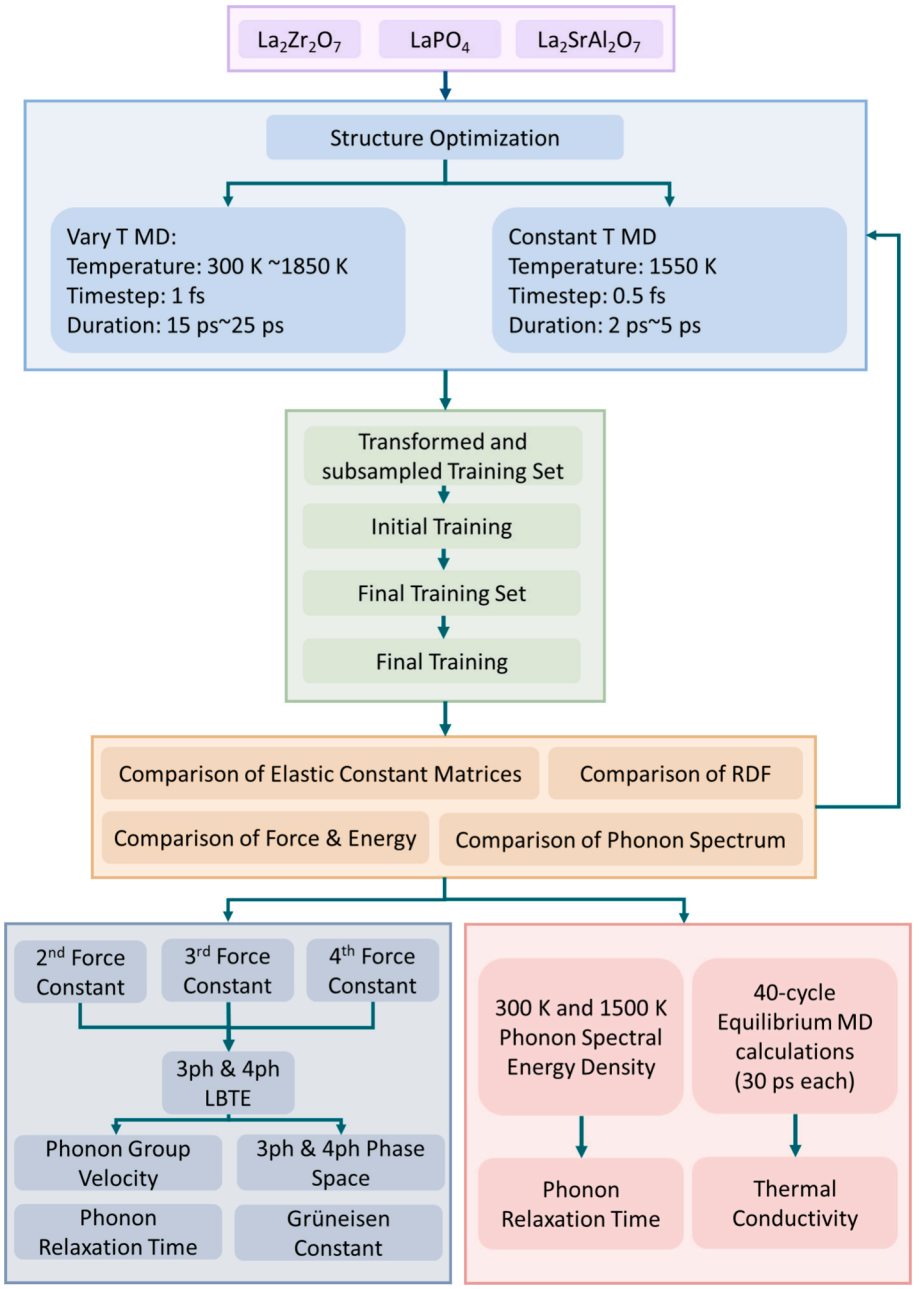

Fig. 1. Overview of the workflow for calculating phonon transport properties of crystalline thermal barrier coatings using machine learning potential.

typically involve the calculation of root mean square errors (RSMEs) for various trained quantities, and comparisons of the structural parameters (equilibrium lattice parameters and atomic radial distribution function) and physical properties (elastic constants and phonon spectrum) obtained using MTPs to those of DFT calculations. In our current workflow, a passive training procedure is adopted where those atomic configurations with high extrapolation degrees are selected and merged with the original training datasets manually. In the final step, the MTPs are used either to obtain higher order force constants from lattice dynamics calculations under the framework of LBTE method or to evaluate the lattice thermal conductivity directly from equilibrium molecular dynamics (EMD) simulations within Kubo-Green formula. In addition, the calculation of phonon spectrum energy density (pSED) from EMD simulations also allows us to extract the phonon quasi-particle lifetimes, showing the effects of multi-phonon scatterings on the phonon heat conduction at various temperatures.

2.2. DFT calculations

All first-principles calculations based on density functional theory (DFT) were carried out using VASP program (version 5.4.4) under the three-dimensional periodic boundary conditions (3D-PBCs) and plane wave basis [30–32]. The projector augmented wave (PAW) method was used to describe the interactions between valence electrons and ionic core [32,33]. The valence electrons considered in this work for the relevant elements were La ($5s^2 5p^6 5d^1 6s^2$), Zr ($4s^2 4p^6 4d^2 5s^2$), Sr ($3s^2 3p^6 4s^2$), Al ($3s^2 3p^1$) and O ($2s^2 2p^4$), respectively. The generalized gradient approximation (GGA) in terms of Perdew-Burke-Ernzerhof (PBE) functional was adopted to calculate exchange–correlation energy of electrons [34]. All calculations were conducted under the non-spin polarized DFT scheme, assuming the spin-compensated paramagnetic state for the studied crystal structures. The kinetic energy cutoff value was set to 600 eV for plane wave expansion in the reciprocal space. Regarding the numerical integration k-meshes, we employed 4 ×

4 × 4, 10 × 10 × 2, and 8 × 8 × 8 grids for the pyrochlore, double perovskite, and monazite structures, respectively. For the static structural optimizations, the total energy (the mean atomic force) was converged to 10^{-8} eV·cell^{-1} (0.001 eV·Å^{-1}). Notably, the conventional cells of the three crystal structures were used, and total numbers of atoms were 88 (cubic-$La_2Zr_2O_7$), 24 (tetragonal-$La_2Sr_2AlO_7$) and 24 (monoclinic-$LaPO_4$), respectively (See Fig. 2).

To perform the first-principles molecular dynamics (FPMD) simulations, the supercells were built for double-perovskite and monazite, i.e., a 3 × 3 × 1 supercell containing 216 atoms for $La_2SrAl_2O_7$ and a 2 × 2 × 2 supercell containing 192 atoms for $LaPO_4$, respectively. While for $La_2Zr_2O_7$, the conventional cell within 88 atoms was used. Otherwise, k-point grids were set to 2 × 2 × 2 for supercells of $LaPO_4$ and $La_2Zr_2O_7$, and the 2 × 2 × 1 mesh was chosen in the case of $La_2SrAl_2O_7$. Two different types of FPMD tasks were conducted to create the required datasets for training and testing machine learning potentials. The constant temperature FPMD simulations at 1550 K were realized using the canonical ensemble (NVT) within the Nosé-Hoover thermostat [35] and the total duration of 3 ps with a time step of 0.5 fs. In the case of the varying temperature FPMD simulations, the annealing molecular dynamics was carried out in the temperature range from 250 K to 1650 K with a total duration of 16 ps and a time step of 1 fs. Visualizations of crystal structures were realized using VESTA program [36].

2.3. Moment tensor potential training and testing

The moment tensor potential adopted in current work is referred to the level 22 potential (MTP-22) with a maximum cutoff radius of 8.0 Å for radial basis functions. Training the MTP-22 potentials for the three crystal structures uses the default values for fitting weights of energy (1.0), forces (0.1) and stress tensors (0.001), and the default fitting scaling parameters (See Table S1). During the learning process of MTP-22, the predicted values of total energy, forces and stress tensors for an atomic configuration are compared to those of quantum–mechanical datasets in FPMD trajectory, and the corresponding RMSEs are calculated. The quality of the trained MTP-22 potential is characterized by the obtained RMSEs. Since a passive learning procedure was used to train MTPs, the training process was splitting into two steps. In the first learning step, the training was conducted for a relatively small number of atomic configurations and their quantum–mechanical datasets for each crystal structure, i.e., less than 1000 atomic configurations sampled from the FPMD trajectory ($> 10^4$ configurations). The resulting MTP model was employed to resample the whole FPMD training datasets. Those atomic configurations with high extrapolation grades were identified, and which were selected and combined with the initial training datasets. In the second step of passive learning, the updated training datasets were employed to retrain the new clean MTP-22 potential. This two-step passive learning procedure was found to be highly efficient for utilizing FPMD configurations to refine the MTP potential [29,37].

2.4. LBTE calculations for phonon transport properties

Solving the LBTE for phonons to obtain the lattice thermal conductivity and phonon scattering phase spaces requires the evaluation of the second, third and even the fourth order interatomic force constants from the lattice dynamics calculations based either on the first-principles method or the machine learning potentials. In this work, the trained MTP-22 potentials for the three prototype thermal barrier coatings were employed to calculate the inter-atomic force constants up to the fourth order using the PhonoLAMMPS interfaced with LAMMPS program [38–40]. Then the temperature renormalized second order force constants were directly used to calculate phonon spectrum within Phonopy code [41,42]. Meanwhile, the third and fourth order force constants were obtained from post-processing python scripts such as Thirdorder.py and Fourthorder.py [43]. Finally, the ShengBTE code was adopted to solve LBTE for phonons under the relaxation time approximation (RTA) [44]. Notably, for calculating higher order force constants (3rd and 4th orders), supercells were built for monazite-$LaPO_4$ and double-perovskite-$La_2SrAl_2O_7$, i.e., 3 × 3 × 1 and 3 × 3 × 3, respectively. While the conventional cell of pyrochlore-$La_2Zr_2O_7$ was adopted in the calculations. Otherwise, we set the q-meshes to 8 × 8 × 5, 7 × 7 × 7, and 4 × 4 × 4 for $La_2SrAl_2O_7$, $LaPO_4$ and $La_2Zr_2O_7$ in LBTE calculations for three-phonon scattering phase space. After considering both three-phonon and four-phonon scattering mechanisms, the q-meshes were adjusted to reduce the heavy computational costs involved in multi-phonon scattering phase space using LBTE method, i.e., 3 × 3 × 2 ($La_2SrAl_2O_7$), 7 × 7 × 7 ($LaPO_4$), and 4 × 4 × 4 ($La_2Zr_2O_7$), respectively.

2.5. Equilibrium molecular dynamics simulations

All equilibrium molecular dynamics (EMD) simulations were conducted using LAMMPS program interfaced with moment tensor potential (MTP) [29]. Performing EMD allows the direct calculation of heat current and its autocorrelation function (HCACF) at a specific temperature, enabling the use of Kubo-Green formula to evaluate the lattice thermal conductivity with the inclusion of all anharmonic effects in the phonon lattice dynamics at finite temperature (See Eq. (1)). This method could in principle fully elucidate the impacts of all higher order phonon–phonon scattering mechanisms on lattice thermal conductivity, compared to LBTE calculations where only 3rd and 4th order atomic force constants were included.

$$\kappa_{EMD} = \frac{1}{3k_B T^2 V}\int_0^{\infty} \langle J(0)\cdot J(t)\rangle dt \tag{1}$$

Here, k_B is the Boltzmann constant, T is the temperature, V is the unit cell volume, $J(0)$ is the heat current, and the $\langle J(0)\cdot J(t)\rangle$ is the heat current autocorrelation function (HCACF).Regarding the computational details in MD simulations within LAMMPS, supercells were created for the relevant crystal structures, i.e., 4 × 4 × 4, 12 × 12 × 2, and 6 × 6 × 6

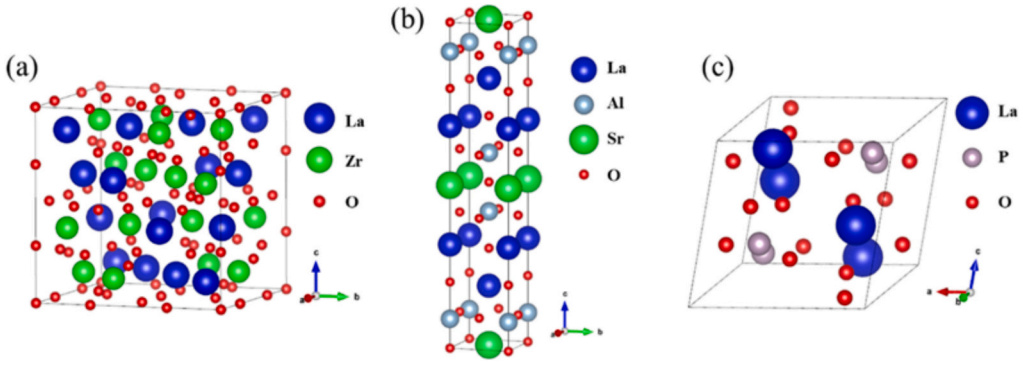

Fig. 2. Crystal structures of (a) pyrochlore $La_2Zr_2O_7$ (b) double-perovskite $La_2SrAl_2O_7$ (c) monazite $LaPO_4$.

supercells for $La_2Zr_2O_7$, $La_2SrAl_2O_7$ and $LaPO_4$, respectively. Before performing the production run for each crystal structure to calculate the HCACF, the supercells were fully relaxed in NPT ensemble for a total duration of 50 ps with the time step of 1 fs. All subsequent EMD simulations were carried out in NVE ensemble with the total duration of 1 ns and a time step of 1 fs, i.e., the total number of time steps was 1.2×10^6. Then, HCACF profiles were calculated from 40 independent MD simulations at the specified temperature to reduce statistical uncertainty. It is worth noting that the HCACF profile for crystalline solids does not decay exponentially to zero at a relatively long correlation time interval. Thus, a truncation time of 30 ps was used for all HCACF calculations. The calculated HCACF profiles were further smoothed using low pass filtering process [23]. Applying the Kubo-Green formula to the smoothed HCACF profiles, the lattice thermal conductivity was obtained from each HCACF profile. In the last step, the mean lattice thermal conductivity was averaged from all 40 trials.

2.6. Phonon spectrum energy density calculations

For crystal structures, the pSED is obtained from the MD trajectory using Eq. (2) [45]. In contrast to those of LBTE calculations for the multi-phonon scattering spaces, pSED could include all anharmonic effects in the phonon scattering processes in a non-perturbative way.

$$\phi\left(\vec{k},\omega\right) = \frac{1}{4\pi N_c \Delta t}\sum_{\alpha}\sum_{l=1}^{p} m_l \left| \int_0^{\Delta t} \sum_{n=1}^{N_c} \nu_{\alpha}^{(n,l)}(t) exp\left[i\left(\vec{k}\cdot\vec{r}^{(n)} - \omega t\right)\right] dt \right|^2 \tag{2}$$

Here, N_c represents the total number of unit cells in the system, Δt is the simulation time, $\vec{r}^{(n)}$ is the equilibrium position of unit cell n, p is the number of atoms in unit cell n, $\nu_{\alpha}^{(n,l)}$ is the velocity of atom l in direction α within unit cell n, m_l is the atomic mass, and $\vec{k}$ is the phonon wave vector.

All molecular dynamics simulations were conducted using the LAMMPS program and the trained MTPs for the investigated thermal barrier coatings in NVT ensemble. The total duration for the production run was set to 1.5 ns with a time step 0.75 fs. For obtaining a relatively smooth pSED profile, the dense k gird must be employed. The number of k points in pSED calculation is determined by the supercell size. In this paper, the supercells of $La_2Zr_2O_7$ and $La_2SrAl_2O_7$ ($LaPO_4$) were chosen as $85 \times 2 \times 1$, and $125 \times 5 \times 1$, respectively. Thus, the total numbers of k-points were 85 and 125 for the relevant crystal structures in the x-direction (or [100] crystallographic direction). Therefore, the pSED was obtained along Γ (0 0 0)-Y (0.5 0 0) pathway in the Brillouin zone.

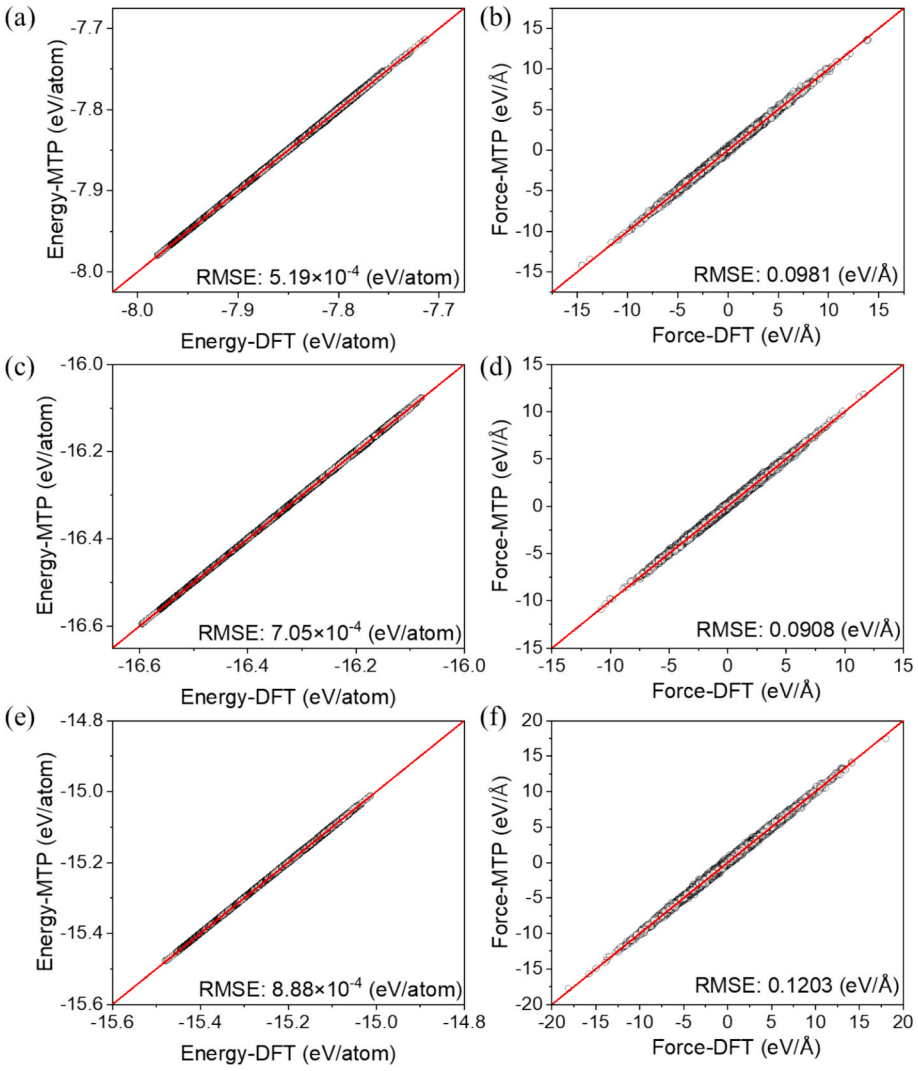

Fig. 3. Testing MTPs for the total energy and atomic forces: (a)-(b) pyrochlore-$La_2Zr_2O_7$; (c)-(d) double perovskite $La_2SrAl_2O_7$; (e)-(f) monazite $LaPO_4$.

3. Results and discussions

3.1. Testing and validation of MTPs

Here, we test the accuracy of the obtained MTPs for the three crystal structures by directly comparing the predicted total energies and atomic forces using MTPs to those of benchmark DFT results in terms of RMSEs. The calculated RSMEs of total energy and forces are presented in Fig. 3. Overall, we observe a very promising agreement between MTP results and the benchmark datasets. Specifically, for the atomic forces, RSMEs are converged to 0.098 eV/Å, 0.091 eV/Å, and 0.120 eV/Å for $La_2Zr_2O_7$, $La_2SrAl_2O_7$ and $LaPO_4$, respectively. While the RSMEs of atomic forces are all reduced to 0.001 eV/atom. The results clearly demonstrate the workflow employed in this work to train the MTPs is highly efficient and robust for crystalline thermal barrier coatings.

The validation of the trained MTPs is performed by evaluating various structural parameters and physical properties of the three crystal structures and comparing the results with those of DFT calculations. First, we show the calculated equilibrium lattice parameters of $La_2Zr_2O_7$, $La_2SrAl_2O_7$ and $LaPO_4$ crystals with both DFT and MTPs in Table 1. An excellent agreement is seen regarding the results of $La_2Zr_2O_7$ and $La_2SrAl_2O_7$ crystal structures, i.e., the mean errors are found to be 0.01 % and 0.11 %, respectively. While the errors are revealed to be relatively large for lattice parameters *b* (5.57 %) and *c* (7.66 %), compared to that of lattice constant *a* (0.01 %) in the case of monazite $LaPO_4$ which has the monoclinic space group. To further improve the accuracy of the trained MTP for predicting the lattice parameters *b* and *c* of monazite $LaPO_4$, additional training datasets from those slightly deformed lattice structures are expected to be included in the training dataset. Since most equilibrium lattice parameters are well reproduced from the MTPs for the three crystal structures, additional refining of MTP for $LaPO_4$ is not conducted. Second, we evaluate the radial distribution functions for the three crystal structures using MTPs and comparing the profiles to those of FPMD simulations at the same temperature. The RDF profiles of MTPs and FPMD simulations are illustrated in Fig. 4 for all relevant structures. Again, we see the profiles of $La_2Zr_2O_7$, $La_2SrAl_2O_7$ and $LaPO_4$ obtained from MTP closely resemble those of FPMD simulations especially for the peak positions in the whole distance range, indicating that all trained MTPs could precisely reproduce the very detailed atomic structures that fully match with those of DFT calculations. Quantitative analysis reveals that the RMSEs for the RDF functions of the three structures are 0.19, 0.15, and 0.18, respectively.

Besides those structural properties (lattice parameters and RDFs), the full set of elastic constants is also calculated for each crystal structure using MTP and DFT, and all results are summarized in Table 2. In general, we find a close agreement of DFT values with those of MTP predictions for diagonal components in the elastic tensors for $La_2Zr_2O_7$, $La_2SrAl_2O_7$ and $LaPO_4$ crystal structures. For some of the off-diagonal tensor components such as C_{26}, C_{36} and C_{45} in monazite $LaPO_4$, the relatively larger errors are indeed obtained. Nevertheless, the actual values of C_{ij} predicted by MTP are close to those of DFT results in the case of $LaPO_4$. Considering all MTPs are trained only using the machine learning datasets of equilibrium lattice structures, the predictive performance of them on the elastic constants is satisfactory for the studied crystal structures.

Table 1
Comparison of lattice constants predicted by DFT and MTPs for $La_2Zr_2O_7$, $La_2SrAl_2O_7$ and $LaPO_4$ crystal structures.

		DFT (Å)	MTP (Å)	Error (%)
$La_2Zr_2O_7$	*a*	10.879	10.880	0.01
	b	10.879	10.880	0.01
	c	10.879	10.878	0.01
$La_2SrAl_2O_7$	*a*	3.782	3.779	0.08
	b	3.782	3.779	0.08
	c	20.628	20.662	0.16
$LaPO_4$	*a*	6.935	6.939	0.06
	b	6.645	7.015	5.57
	c	6.541	7.042	7.66

3.2. Renormalization of phonon spectrum

The phonon spectra of the three structures calculated by DFT and MTP are shown in Fig. 5 while the PDOS obtained from MTP is presented in Fig. S1. In the cases of $La_2Zr_2O_7$ and $La_2SrAl_2O_7$, as shown in Fig. 5(a) and 5(b), both approaches predict no imaginary phonon modes in the Brillouin zone. While the phonon spectrum of $LaPO_4$ obtained from the standard harmonic lattice dynamics at 0 K within DFT exhibits strong soft modes in both acoustic and optical branches, compared to the full elimination of all soft modes in the results of MTP, as shown in Fig. 5(c). Notably, we see the close agreement for all phonon dispersions between MTP and DFT results for pyrochlore $La_2Zr_2O_7$, indicating the relatively weak renormalization of interatomic force constants at finite temperature for this crystal structure. Otherwise, the results for $La_2SrAl_2O_7$ imply the strong influence of temperature on the normalized phonon frequencies especially for those optical modes in the whole Brillouin zone. Interestingly, the phonon dispersions predicted by MTP move to higher frequencies than those of DFT calculations at 0 K for $La_2SrAl_2O_7$. The stiffening of optical modes is expected to impact the phonon scattering rates and lattice thermal conductivity at relatively high temperatures. It is also worth noting that the advantage of using MTP to conduct the lattice dynamics embedded with temperature renormalization of inter-atomic force constants is clearly demonstrated for monazite $LaPO_4$ where the standard harmonic approximation fails to predict its dynamic structure stability, while MTP results show no soft modes in the phonon spectrum. Furthermore, the LBTE method may also not be applicable to $LaPO_4$ due to the presence of multiple soft phonon modes under the conventional harmonic approximation at 0 K. Therefore, all subsequent calculations for higher order interatomic force constants, 3ph + 4ph phonon scattering rates and lattice thermal conductivity of $La_2Zr_2O_7$, $La_2SrAl_2O_7$ and $LaPO_4$ crystal structures are conducted within the temperature renormalized phonon spectra under perturbative LBTE framework.

3.3. Three and four-phonon scattering mechanisms

Using the temperature renormalized higher order interatomic force constants under the LBTE methodology, the multi-phonon scattering mechanisms including the 3rd and 4th order scattering processes of $La_2Zr_2O_7$, $La_2SrAl_2O_7$ and $LaPO_4$ crystal structures are elucidated in Fig. 6. First, we notice the formation of phonon band gaps either among those optical branches or between optical and acoustic branches could impact the phonon scattering spaces and their dependence on the renormalized phonon frequencies for thermal barrier coatings. In Fig. 6 (a) and 6(c), both three and four-phonon scattering spaces are illustrated for $La_2Zr_2O_7$ and $La_2SrAl_2O_7$, and the results show that multi-phonon interactions decrease with the increase of phonon frequency. Such a trend, which is mainly determined by the redistribution process (See Figs. S2(d) and S2(e)), is quite strong for four-phonon scattering space in both crystal structures, compared to that of three-phonon scatterings (See Figs. S2(a) and S2(b)). In the case of $LaPO_4$, the presence of multiple phonon band gaps among those optical phonon branches lead to the segmented three and four-phonon scattering spaces versus the frequency, as shown in Fig. 6(e). Nevertheless, the overall scattering space for three or four-phonon interactions is found to decrease with the increment of frequency for $LaPO_4$, and the finding is like that of either $La_2Zr_2O_7$ or $La_2SrAl_2O_7$. Second, the four-phonon scattering space seems to be significantly impacted by the number of atoms in the conventional

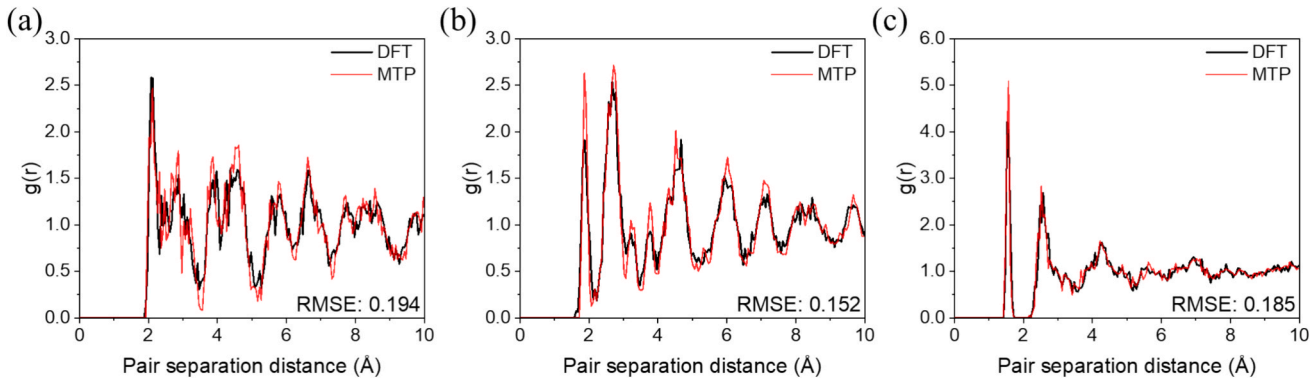

Fig. 4. The calculated radial distribution functions (RDF) of the three crystal structures from MD simulations based on DFT and MTPs: (a): $La_2Zr_2O_7$; (b): $La_2SrAl_2O_7$; (c): $LaPO_4$.

Table 2
Comparison of elastic constants predicted by DFT and MTPs for $La_2Zr_2O_7$, $La_2SrAl_2O_7$ and $LaPO_4$ crystal structures and the calculated errors of MTP results.

		DFT (GPa)	MTP (GPa)	Error (%)
$La_2Zr_2O_7$	C_{11}	271.04	260.79	3.78
	C_{12}	126.93	108.17	14.78
	C_{44}	87.89	85.37	2.87
$La_2SrAl_2O_7$	C_{11}	263.32	280.15	6.39
	C_{12}	106.81	101.52	4.95
	C_{13}	126.96	119.17	6.13
	C_{33}	218.97	209.56	4.30
	C_{44}	124.15	116.48	6.18
	C_{66}	111.22	122.85	10.46
$LaPO_4$	C_{11}	144.28	148.62	3.01
	C_{12}	58.53	68.39	16.85
	C_{13}	76.98	80.45	4.44
	C_{16}	9.43	11.28	19.62
	C_{22}	182.33	189.16	3.75
	C_{23}	76.98	81.91	6.40
	C_{26}	12.32	15.43	25.44
	C_{33}	224.2	223.6	0.27
	C_{36}	−11.62	−9.46	18.59
	C_{44}	39.95	39.09	2.15
	C_{45}	8.95	10.64	18.89
	C_{55}	49.59	51.39	3.63
	C_{66}	52.13	50.68	2.726

cell of thermal barrier coatings rather than the crystal symmetry. From Fig. 6(a), 6(c) and 6(e), we can easily find that the scattering spaces of $La_2Zr_2O_7$, $La_2SrAl_2O_7$ and $LaPO_4$ are 4.5–2.0 × 10^{-6}, 2.5–1.2 × 10^{-6} and 1.3 × 10^{-6}–5.0 × 10^{-7}, respectively. The results clearly indicate that reducing the total number of optical phonon branches in the crystal structure with a small conventional cell is effective to suppress the multi-phonon scatterings regardless of the crystal symmetry. From such a perspective, the pyrochlore crystal structure with a large conventional cell is predicted to exhibit large three and four-phonon scatterings, probably leading to smaller lattice thermal conductivity, compared to that of $La_2SrAl_2O_7$ or monazite $LaPO_4$. The impact of three and four-phonon scatterings on the phonon relaxation times are further investigated, and the results are plotted in Fig. 6(b), 6(d) and 6(f) for $La_2Zr_2O_7$, $La_2SrAl_2O_7$ and $LaPO_4$, respectively. In structures like $La_2Zr_2O_7$ and $La_2SrAl_2O_7$, three and four-phonon scatterings give similar relaxation times in the whole frequency range. However, the obtained phonon relaxation times of $La_2Zr_2O_7$ are in the range from 0.1 ps–2.0 ps, compared to 0.1 ps–10 ps of $La_2SrAl_2O_7$, as can be seen from Fig. 6(b) and 6(d). The results again demonstrate the dominance of optical phonon branches in pyrochlore $La_2Zr_2O_7$ (88 atoms in conventional cells) could substantially reduce the phonon relaxation times due to the large multi-phonon scattering spaces. In comparison, inclusion of four-phonon scattering mechanism results in the smaller phonon relaxation times, compared to those of three-phonon scattering process only. In addition, the predicted phonon relaxation times of monazite $LaPO_4$ are shown in Fig. 6(f), and the values are found to be in the range from 0.2 ps–5.0 ps, and which are situated between those of $La_2Zr_2O_7$ and $La_2SrAl_2O_7$. Finally, it is also worth noting that all results presented in Fig. 6 are expected to reflect the phonon scattering spaces versus frequency distributions of the three thermal barrier coatings under both 3ph and 3ph + 4ph schemes qualitatively, because the relatively coarse k-meshes are employed for all crystal structures to avoid the formidable computational costs.

Besides phonon scattering spaces and relaxation times, the phonon mode resolved Grüneisen parameters and group velocities are also evaluated, and all results are given in Fig. S3 for the three crystal structures. The phonon mode averaged Grüneisen parameters and phonon group velocities are shown in Fig. 7 for all studied crystal

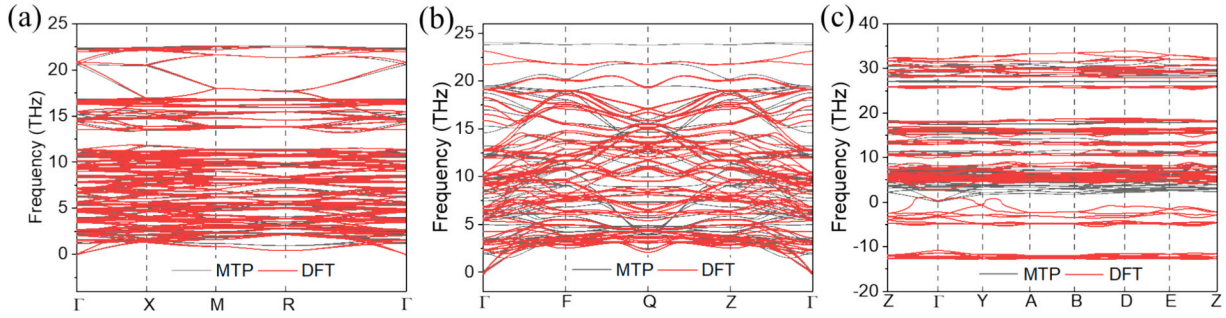

Fig. 5. The calculated phonon spectra of the three prototype thermal barrier coatings using DFT and MTPs: (a) pyrochlore $La_2Zr_2O_7$; (b) double perovskite $La_2SrAl_2O_7$; (c) monazite $LaPO_4$.

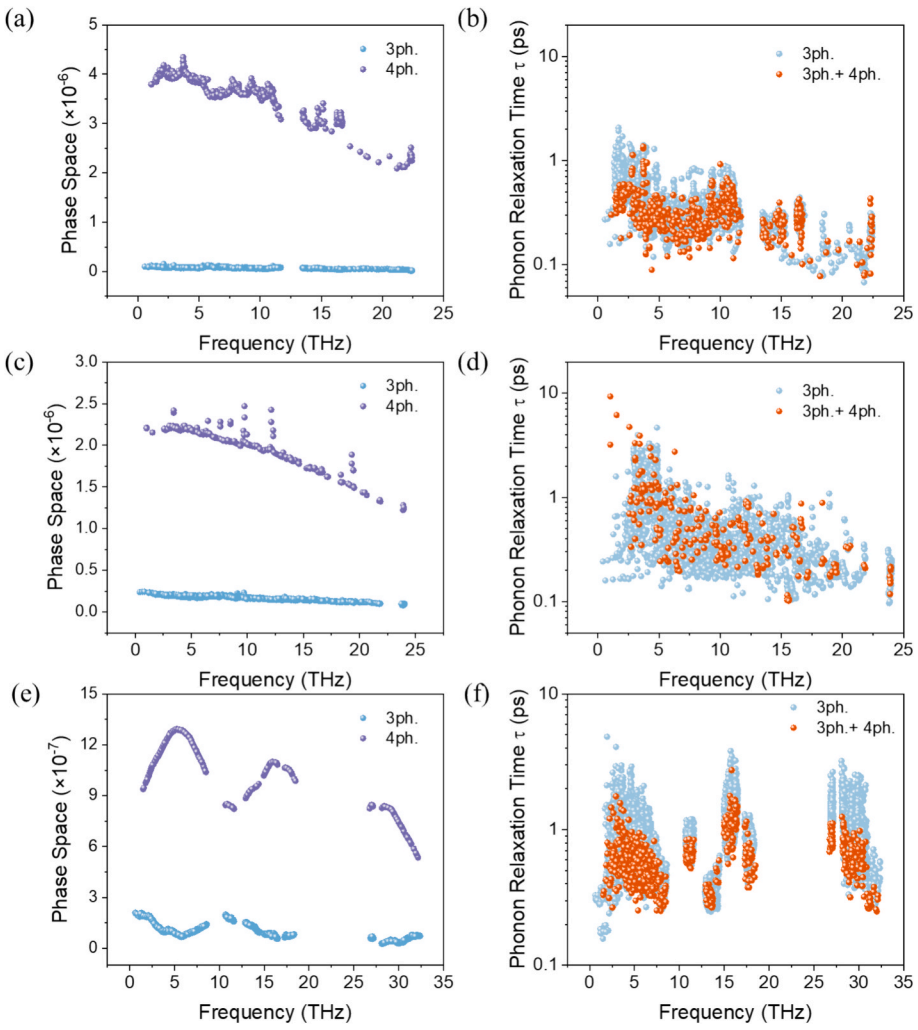

Fig. 6. Phonon scattering spaces and relaxation times with the inclusion of three and four-phonon scattering processes for the three crystal structures: (a)-(b) $La_2Zr_2O_7$; (c)-(d) $La_2SrAl_2O_7$; (e)-(f) $LaPO_4$. Note that different k-meshes are employed for relevant crystal structures using 3ph and 3ph + 4ph schemes.

structures. As shown in Fig. 7(a), the mean Grüneisen parameters are decreased in the order of $La_2Zr_2O_7$, $La_2SrAl_2O_7$ and $LaPO_4$. The values of $La_2Zr_2O_7$ (~1.99) and $La_2SrAl_2O_7$ (~1.95) are significantly larger than that of $LaPO_4$ (~0.7). After the inclusion of four-phonon scattering mechanism, the mean Grüneisen parameter of $LaPO_4$ remains the lowest among the three crystal structures. Overall, we may conclude that the lattice anharmonicity of $LaPO_4$ is weaker than that of either $La_2Zr_2O_7$ or $La_2SrAl_2O_7$. This conclusion is fully consistent with the observation that the 3ph and 4ph scattering spaces of $LaPO_4$ are smaller than those of pyrochlore and double perovskite especially for the 4ph scatterings. The calculated mean phonon group velocities of the three crystal structures are plotted in Fig. 7(b). It is revealed that $La_2SrAl_2O_7$ gives the larger mean group velocity than that of pyrochlore and double perovskite, i.e., 1.58 km/s versus 0.6–0.7 km/s. When both three and four-phonon scatterings are considered in calculations, the mean group velocities of $La_2Zr_2O_7$ and $LaPO_4$ are increased slightly. While the mean velocity of $La_2SrAl_2O_7$ is reduced under 3ph + 4ph scheme, compared to that of 3ph only case. The obtained relatively large phonon group velocity of $La_2SrAl_2O_7$ is also reflected in the calculated phonon spectrum, as shown in Fig. 5(b). From the phonon transport kinetic theory, the small phonon

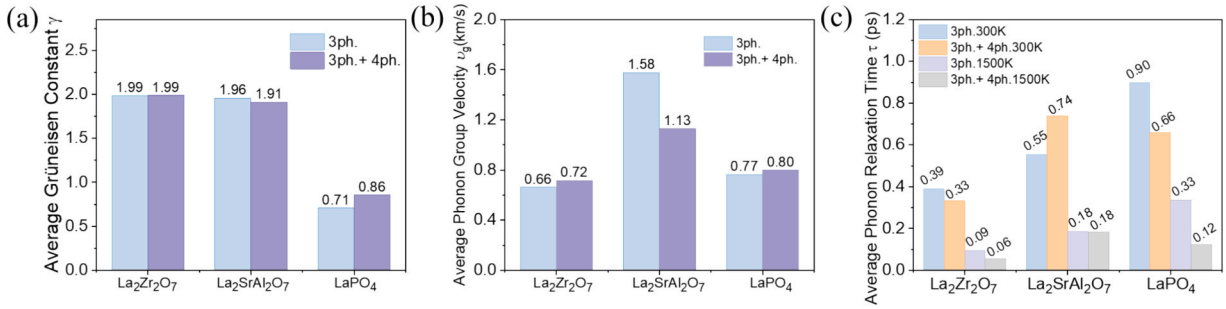

Fig. 7. The calculated mean values of phonon properties for the three crystal structures under 3ph and 3ph + 4ph scattering schemes in perturbative LBTE method: (a) Grüneisen constant at 300 K; (b) group velocities; (c) relaxation times at 300 K and 1500 K.

group velocity and large multi-phonon scattering space would directly lead to low lattice thermal conductivity. Among all studied three prototype thermal barrier coatings, the pyrochlore $La_2Zr_2O_7$ has the smallest mean phonon group velocity and the largest phonon scattering spaces (3ph or 3ph + 4ph), all favoring the reduction of lattice thermal conductivity.

The effects of temperature on the phonon mean relaxation times are calculated at 300 K and 1500 K, and the results are displayed in Fig. 7(c). At 300 K, the mean phonon relaxation times are predicted to increase in the order of $La_2Zr_2O_7$, $La_2SrAl_2O_7$ and $LaPO_4$ under 3ph scattering scheme. Interestingly, the 3ph + 4ph scheme predicts the change of the order to $La_2Zr_2O_7$, $LaPO_4$ and $La_2SrAl_2O_7$ at the same temperature. Therefore, the current LBTE calculations for $La_2SrAl_2O_7$ based on the temperature normalized atomic force constants predict a reduction of multi-phonon scattering spaces and the lattice anharmonic effects within 3ph + 4ph method at room temperature. Meanwhile, lattice anharmonicity of either $La_2Zr_2O_7$ or $LaPO_4$ is enhanced after considering 3ph + 4ph processes.

For all three crystal structures, raising the temperature from 300 K to 1500 K significantly reduces the phonon mean relaxation times under both 3ph and 3ph + 4ph schemes, as shown in Fig. 7(c). Notably, the mean phonon relation times of $La_2Zr_2O_7$ and $LaPO_4$ are further decreased in 3ph + 4ph scheme, compared to those of 3ph mechanism at 1500 K. While the 3ph and 3ph + 4ph schemes give the same phonon mean relaxation times in the case of $La_2SrAl_2O_7$. As a result, the $La_2SrAl_2O_7$ has the largest mean phonon relaxation time among all three crystal structures under the 3ph + 4ph scheme at 1500 K. The results displayed in Fig. 7(c) also revealed that the pyrochlore $La_2Zr_2O_7$ also gives the smallest mean phonon relaxation time along the three crystal structures regardless of the temperature and the employed multi-phonon scattering schemes.

Previous studies on the phonon transport properties of pyrochlore-$La_2Zr_2O_7$ and monazite-$LaPO_4$ have concluded that the phonon mean-free paths of many optical modes in those crystal structures are already below the Ioffe-Regel cutoff value, requiring a distinction of propagons, diffusons and locons among all phonon modes [17,46]. In this paper, the participation ratio (*PR*) is calculated from Eq. (3), using phonon eigenvectors ($\vec{e}_{i,n}$) based on the temperature renormalized phonon spectrum for each crystal structure. Note that in Eq. (3), the N runs over all atoms in the conventional cell of the crystal structure. By the definition of *PR* in Eq. (3), a fully extended phonon mode (propagon or diffuson) gives $PR = 1$, while the fully localized phonon mode has $PR = 1/N$ [17,18,47]. Typically, the locons are identified as $PR < 0.1$.

$$PR_n = \frac{\left(\sum_i \vec{e}^{\,2}_{i,n}\right)^2}{N\sum_i \vec{e}^{\,4}_{i,n}} \tag{3}$$

The calculated PRs for all three crystal structures are plotted in Fig. 8. Here, we find that locons in pyrochlore-$La_2Zr_2O_7$ are distributed in a wide range versus frequency, including both acoustic phonon branches below 2.5 THz, and those optical modes above 1.2 THz (See Fig. 5(a)). Nevertheless, a large portion of phonon modes in the same frequency range are also attributed to propagons, because many of them show PRs larger than 0.1. Meanwhile, the PRs of either $La_2SrAl_2O_7$ or $LaPO_4$ are less than 0.1 for almost all optical phonon modes, implying the dominance of locons in the optical phonon branches. Below 5.0 THz, the presence of acoustic phonon branches contributes to the observed large PRs in $La_2SrAl_2O_7$ and $LaPO_4$. Thus, extended lattice vibrations are mainly concentrated in the acoustic phonon modes in the cases of double perovskite and monazite. Overall, besides all extended phonon modes (propagons), those highly localized phonon modes in terms of locons are expected to play an important role in determining intrinsic lattice thermal conductivity of the three prototype thermal barrier coatings. The standard LBTE approach is reliable to describe the phonon transport properties of lattice wave like phonon modes or propagons, and which could strongly underestimate the lattice thermal conductivity attributing to localized phonon modes (locons or diffusons) [20,48]. One probable treatment to improve the accuracy of LBTE method is to employ the Wigner's formula for all localized phonon modes (diffusons and locons) under the perturbative theoretical framework for calculating the lattice anharmonicity [20,46]. However, combing the equilibrium molecular dynamics simulations and Kubo-Green formula with the temperature renormalized inter-atomic forces in terms of MTPs may be computationally more feasible for complex crystal structures with either a large conventional cell or the low crystal symmetry such as pyrochlore and monazite studied in this work.

3.4. Intrinsic lattice thermal conductivity

Here, two distinct approaches, which are referred to perturbative LBTE and EMD-KG methods, are applied to evaluate the intrinsic lattice thermal conductivity of the three crystal structures at the finite temperatures between 300 K and 1500 K. While the calculations are not conducted below 300 K because the EMD-KG method is based on classic molecular dynamics simulation where the phonon distribution shows better agreement with Bose-Einstein distribution only at relatively high temperature [49]. Otherwise, the operational temperature of thermal barrier coatings in the engineering applications is anticipated to be significantly higher than the room temperature.

The calculated lattice thermal conductivities of $La_2Zr_2O_7$, $La_2SrAl_2O_7$ and $LaPO_4$ between 300 K and 1500 K using LBTE and EMD-KG methods are illustrated in Fig. 9 together with the available experimental results. The convergence behaviors of EMD-KG calculations associated with Fig. 9 are provided in Fig. S4, S5, and S6. For all the crystal structures investigated, the 3ph + 4ph scheme always predicts a lower lattice thermal conductivity in the whole temperature range, compared to that of 3ph approach under LBTE method. Thus, the inclusion of four-phonon scattering processes in LBTE method further suppresses the intrinsic thermal conductivity of all three crystal structures, because the overall multi-phonon scattering space is larger in 3ph

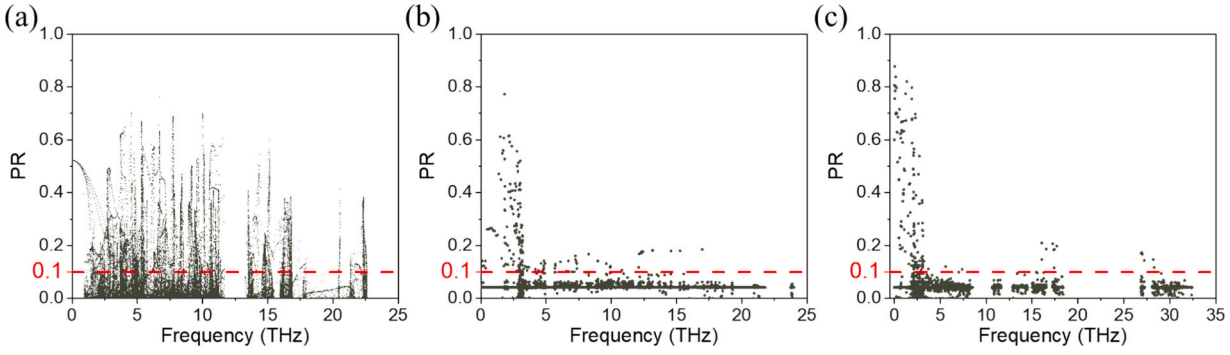

Fig. 8. The calculated participation ratios of phonon modes: (a): $La_2Zr_2O_7$; (b): $La_2SrAl_2O_7$; (c): $LaPO_4$.

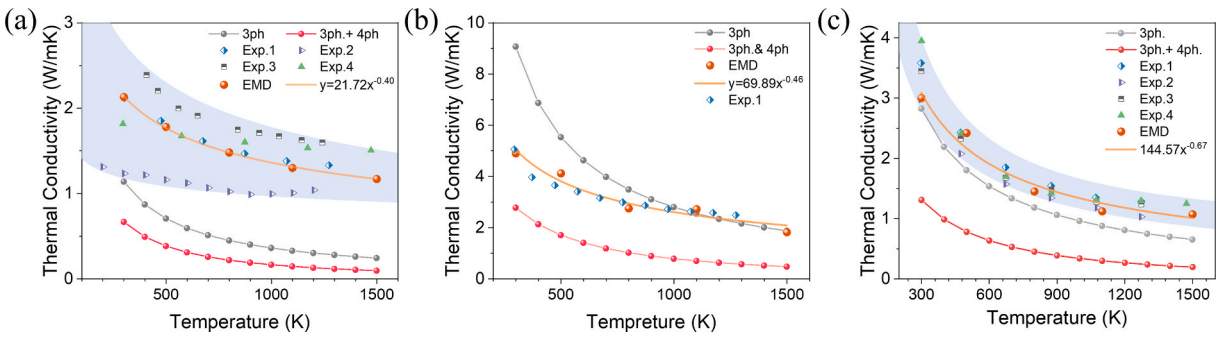

Fig. 9. A comparison of the calculated lattice thermal conductivity of each crystal structure using LBTE method or Kubo-Green formula with that of experimental results in a temperature range from 300 K to 1500 K: (a) $La_2Zr_2O_7$ [50–53]; (b) $La_2SrAl_2O_7$ [54]; (c) $LaPO_4$ [55–58].

+ 4ph scheme than that of 3ph process only. When comparing to the experimental results, LBTE approach underestimates the lattice thermal conductivity of either $La_2Zr_2O_7$ or $LaPO_4$ even under 3ph scattering mechanism alone. Otherwise, bringing the 4ph scattering processes in 3ph + 4ph scheme worsens the agreement between the calculated values and the experimental results, as shown in Fig. 9(a) and 9(c) for $La_2Zr_2O_7$ and $LaPO_4$, respectively. In the case of $La_2SrAl_2O_7$, only considering 3ph scatterings in the LBTE approach, the lattice thermal conductivity is overestimated below 1000 K; while the agreement between experiments and theory is improved above 1000 K (See Fig. 9(b)). After the inclusion of 4ph scatterings in 3ph + 4ph scheme, the calculated lattice thermal conductivity of $La_2SrAl_2O_7$ is too low, compared to that of experimental value at a specified temperature. Overall, we conclude that the LBTE approach under either 3ph or 3ph + 4ph scattering scheme is unable to accurately predict the intrinsic lattice thermal conductivity of the three prototype crystal structures as thermal barrier coatings. Notably, Feng and coworkers suggested that incorporating the Wigner's formula in LBTE method could improve the accuracy of the approach at the high temperature where the localized phonon modes (PR < 0.1) contribute significantly to the lattice thermal conductivity [20].

Regarding the results obtained from EMD-KG method, the good agreement between theory and the experiments is found for all three crystal structures in the whole temperature range, as can be seen from Fig. 9. Compared to that of LBTE method, we see the improvement in numerical accuracy for the lattice thermal conductivity is systematic using EMD-KG method, indicating the high reliability of using EMD-KG method is supported by the sound underlying physics. Typically, the success of EMD-KG method is mainly attributed to the inclusion of all higher order phonon anharmonic effects and their scattering processes in the non-perturbative fashion within the highly accurate MTPs [20,21].

In the literature, another interesting observation is the flattening of experimental lattice thermal conductivity at high temperatures for those thermal barrier coatings, resulting in a strong deviation of the value from the usual 1/T relationship under the three-phonon Umklapp scattering mechanism [59]. In Fig. 9, it is seen that such a flattening of lattice thermal conductivity occurs for all three crystal structures at different temperature ranges, i.e., >800 K for $La_2Zr_2O_7$ and $La_2SrAl_2O_7$, and >1000 K for $LaPO_4$. For structures like $La_2SrAl_2O_7$ and $LaPO_4$, the 3ph + 4ph scheme could predict a flattening of lattice thermal conductivity at high temperatures, compared to that of 3ph method in LBTE approach, as shown in Fig. 9(b) and 9(c). In the case of $La_2Zr_2O_7$, both 3ph and 3ph + 4ph schemes show flat lattice thermal conductivity at elevated temperatures (See Fig. 9(a)). The results suggest that the flat temperature dependence of lattice thermal conductivity in thermal barrier coatings is originated from the higher order phonon anharmonic effects in the perturbative LBTE approach. It is striking to see that the flat thermal conductivity for all three crystal structures is well-reproduced at high temperatures using EMD-KG method in combination with highly reliable MTPs, compared to experimental results. Here, we use $1/T^x$ relationship to fit both experimental data and the calculated profiles in the whole temperature range between 300 K and 1500 K. The fitting curves are also displayed in Fig. S7 for each case. For all experimental datasets, we find $1/T^{0.34}$ ($La_2Zr_2O_7$) [53], $1/T^{0.46}$ ($La_2SrAl_2O_7$) [54] and $1/T^{0.75}$ ($LaPO_4$) [26]. For comparison, those fittings give $1/T^{0.37}$ ($La_2Zr_2O_7$), $1/T^{0.47}$ ($La_2SrAl_2O_7$) and $1/T^{0.67}$ ($LaPO_4$) using the calculated values from EMD-KG method. Overall, the EMD-KG method when combining with an accurate force field is highly promising for quantitively predict the lattice thermal conductivity of thermal barrier coatings above the room temperature.

3.5. Phonon spectral energy density

To further rationalize the promising performance of EMD-KG approach for evaluating the lattice thermal conductivity of thermal barrier coatings, the phonon quasiparticle spectra of $La_2Zr_2O_7$, $La_2SrAl_2O_7$ and $LaPO_4$ in terms of spectral energy density are calculated at 300 K and 1500 K, respectively. The results for the three crystal structures are shown in Fig. 10 along with the temperature renormalized phonon spectrum. At both 300 K and 1500 K, those lower-lying acoustic branches are clearly visible in the calculated pSED for each crystal structure. For those optical phonon branches, the phonon band gaps are also reproduced in the pSED for $La_2Zr_2O_7$ and $LaPO_4$ at 300 K (See Fig. 10(a)-(c) and 10(g)-10(i)). While the results for $La_2SrAl_2O_7$ show more flat phonon quasi-particle dispersions in the pSED at 300 K, compared to the renormalized phonon spectrum, as seen from Fig. 10 (d)-10(f). The predicted pSED at 1500 K for all three crystal structures exhibits the strong broadening and overlapping of optical phonon bands, indicating either the enhanced anharmonic effects or phonon eigenvectors of optical modes are poorly defined at such a high temperature [20,45]. In the case of $LaPO_4$, we also observe the softening of several flat optical phonon bands right below 2.5 THz, and those flat quasi-particle bands directly interference with the acoustic branches. On the other hand, the acoustic phonon quasi-particle bands of $La_2SrAl_2O_7$ are found to be rather stiff and robust against the raising of temperature, as illustrated in Fig. 10(e) and 10(f) at 300 K and 1500 K, respectively. Since the acoustic phonon bands are mainly responsible for the lattice thermal conduction in those thermal barrier coatings, the high resilience of acoustic phonon bands plays the key role in the observed flat thermal conductivity at elevated temperatures.

We further extract the phonon quasi-particle lifetimes using the calculated pSED at 300 K and 1500 K for the three crystal structures, and the results are plotted together with those of temperature renormalized phonon relaxation times computed from perturbative LBTE method under both 3ph and 3ph + 4ph schemes in Fig. 11. It is worth mentioning that the phonon quasi-particle lifetimes are obtained by fitting each individual quasi-particle peak in a pSED line profile with a Lorentzian function. The fitting gives the peak position and line width for a phonon quasi-particle peak. Then the phonon quasi-particle frequency and the lifetime (from Heisenberg uncertainty principle) are

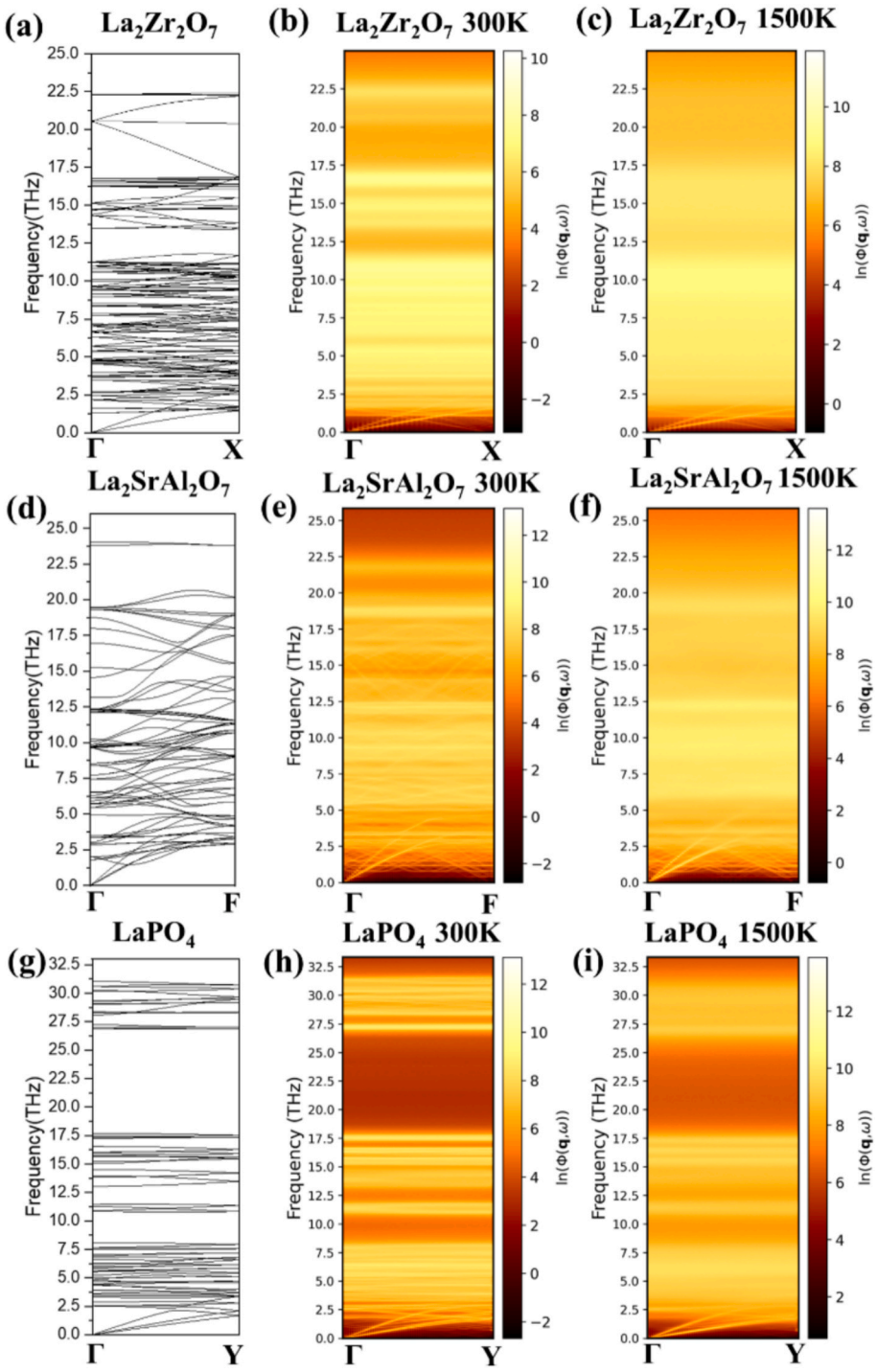

Fig. 10. The calculated phonon spectral energy density (pSED) at 300 K and 1500 K, and the temperature renormalized phonon spectrum: (a)-(c) $La_2Zr_2O_7$; (d)-(f) $La_2SrAl_2O_7$; (g)-(i) $LaPO_4$.

obtained. The fittings are performed for dozens of pSED line profiles that are selected at different q-points in Fig. 11. For the sake of brevity, all fitting curves and results are provided in Figs. S8-S13 for $La_2Zr_2O_7$, $La_2SrAl_2O_7$ and $LaPO_4$, respectively.

From Fig. 11, it is easy to conclude that the predicted phonon quasi-particle lifetimes from the equilibrium molecular dynamics simulations based on MTPs are significantly larger than those of LBTE method under both 3ph and 3ph + 4ph schemes in the whole frequency range. Specifically, the underestimation of the phonon relaxation times using 3ph or 3ph + 4ph schemes is quite significant for acoustic modes below 2.0 THz, resulting in the overall underestimation of lattice thermal conductivity for the studied crystal structures (See Fig. 9). Regarding the effects of temperature on the phonon quasi-particle lifetimes, the decreasing of values is clearly visible in Fig. 11 for all three structures at the elevated temperature. For example, the phonon quasi-particle lifetimes of $La_2Zr_2O_7$ span in a range from 2000 ps to 1 ps at 300 K, while the range is shifted to 300 ps–0.1 ps at 1500 K, as shown in Fig. 11 (a) and 11(b). Meanwhile, $La_2SrAl_2O_7$ gives 2–1000 ps and 1–800 ps at 300 K and 1500 K, respectively (See Fig. 11(c) and 11(d)). Finally, for $LaPO_4$, we find 9–2000 ps at 300 K, and 0.7–700 ps at 1500 K from Fig. 11(e) and 11(f). Therefore, the phonon scatterings of $La_2Zr_2O_7$ and $LaPO_4$ are stronger than those of $La_2SrAl_2O_7$ at high temperatures. Moreover, the

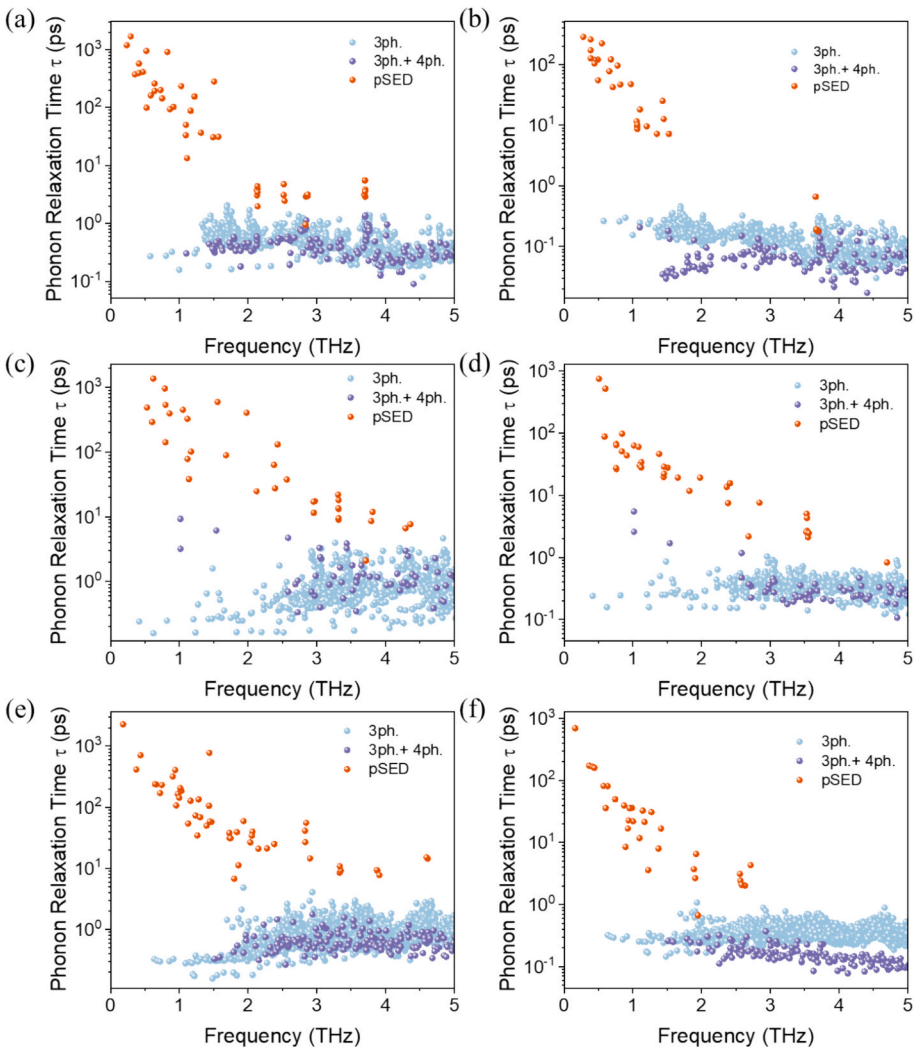

Fig. 11. A comparison of the calculated phonon quasi-particle lifetimes with those of LBTE results under 3ph and 3ph + 4ph schemes at 300 K and 1500 K: (a)-(b) $La_2Zr_2O_7$; (c)-(d) $La_2SrAl_2O_7$; (e)-(f) $LaPO_4$.

predicted mean phonon group velocity of either $La_2Zr_2O_7$ or $LaPO_4$ is substantially smaller than that of $La_2SrAl_2O_7$. As a result, $La_2SrAl_2O_7$ gives a higher lattice thermal conductivity than $La_2Zr_2O_7$ or $LaPO_4$. Notably, the pyrochlore $La_2Zr_2O_7$, owing to the large conventional cell, small phonon group velocity and phonon quasi-particle lifetimes, deliveries the lowest lattice thermal conductivity among all three prototypes thermal barrier coatings for the temperature between 300 K and 1500 K.

4. Conclusions

We have successfully proposed and tested a highly efficient workflow based on tensor potentials (MTPs) to reliably predict lattice thermal conductivity of thermal barrier coatings above the room temperature using either the perturbative LBTE method or the EMD-KG approach. Using the workflow, the temperature renormalized phonon spectra, multi-phonon scattering spaces, the phonon relaxation times, phonon quasi-particle spectra and the quais-particle lifetimes were thoroughly investigated for the three prototypes thermal barrier coatings including $La_2Zr_2O_7$, $La_2SrAl_2O_7$ and $LaPO_4$. It was revealed that the perturbative LBTE approach with the inclusion of 3ph or 3ph + 4ph scattering schemes always results in an underestimation of the lattice thermal conductivity of the three crystal structures, compared to experiments. Moreover, the perturbative LBTE method under the 3ph + 4ph scattering scheme only worsens the agreement between theory and experimental results. The failure of perturbative LBTE approach was found to be related to the presence of a large fraction of highly localized phonon modes (locons) in a wide frequency range especially among those optical phonon branches. The non-perturbative method such as EMD-KG method predicted that the scaling laws of lattice thermal conductivity versus temperature as $1/T^{0.37}$ ($La_2Zr_2O_7$), $1/T^{0.48}$ ($La_2SrAl_2O_7$) and $1/T^{0.67}$ ($LaPO_4$) in the temperature range between 300 K and 1500 K, and which are in good agreement with experimental findings. The calculations of phonon quasi-particle spectrum in terms of spectrum energy density showed that phonon quasi-particle lifetimes obtained from non-perturbative EMD simulations are significantly higher than those of perturbative LBTE methods (3ph and 3ph + 4ph schemes) at elevated temperatures, leading to a more accurate prediction of lattice thermal conductivity for all three crystal structures within the former method. Our results demonstrated that the non-perturbative EMD-KG method combined with machine learning potential provides a highly efficient methodology not only to reliably predict the lattice thermal conductivity but also for a better understanding of multi-phonon scattering mechanism and temperature renormalization effects in thermal barrier coatings.

CRediT authorship contribution statement

Huaxuan He: Writing – review & editing, Methodology, Investigation, Formal analysis, Data curation, Conceptualization. **Xingming Wang:** Visualization, Investigation, Data curation. **Yuzhou Hao:** Methodology, Formal analysis, Data curation. **Chao Zeng:** Visualization, Formal analysis. **Jianyu Li:** Visualization, Formal analysis. **Haoliang Liu:** Methodology, Formal analysis. **Zhibin Gao:** Supervision, Resources. **Jing Feng:** Supervision, Resources, Funding acquisition. **Bing Xiao:** Writing – review & editing, Resources, Project administration, Funding acquisition, Formal analysis, Conceptualization.

Declaration of competing interest

The authors declare that they have no known competing financial interests or personal relationships that could have appeared to influence the work reported in this paper.

Acknowledgements

Bing Xiao would like to acknowledge the financial supports from multiple research grants: the Research Funds of Kunming University of Science and Technology of China (No. 20240391), the Fundamental Research Funds of the Central Universities (No. xtr052024009) and the "Young Talent Supporting Program" of Xi'an Jiaotong University (No. DQ1J009). Zhibin Gao acknowledges the support of the National Natural Science Foundation of China (No. 52250191) and the support of the Key Research and Development Program of the Ministry of Science and Technology (No. 2023YFB4604100). Jing Feng is supported by Yunnan Fundamental Research Projects (grant NO. 202305AS350018). The High-Performance Computing Center at Xi'an Jiaotong University is also acknowledged for the computational hardware support to this work.

Appendix A. Supplementary data

Supplementary data to this article can be found online at https://doi.org/10.1016/j.commatsci.2025.113954.

Data availability

Data will be made available on request.

References

[1] M. Cerit, M. Coban, Temperature and thermal stress analyses of a ceramic-coated aluminum alloy piston used in a diesel engine, Int. J. Therm. Sci. 77 (2014) 11–18.
[2] S.S. Moorthi, M.V. Kumar, M. Prakash, R.S. Kumar, P. Muthuchari, K. Haribabu, Effect of thermal barrier coating of piston on the performance of diesel engine, Mater. Today: Proceed. (2023).
[3] V. Reghu, A. Basha, K. Lobo, S. Shivakumar, P. Tilleti, V. Shankar, P. Ramaswamy, Investigation on thermal barrier effects of 8YPSZ coatings on Al-Si alloy and validation through simulation, Mater. Today: Proceed. 19 (2019) 630–636.
[4] A.D. Porfyris, A. Vafeiadis, C.I. Gkountela, C. Politidis, G. Messaritakis, E. Orfanoudakis, S. Pavlidou, D.M. Korres, A. Kyritsis, S.N. Vouyiouka, Flame-retarded and heat-resistant PP compounds for halogen-free low-smoke cable protection pipes (HFLS Conduits), Polymers 16 (2024) 1298.
[5] P.K. Shukla, E.H. Rao, E. Vetrivendan, R.S. Anne, S.K. Das, B. Malarvizhi, D. Ponraju, B. Nashine, U.K. Mudali, P. Selvaraj, Evaluation of plasma sprayed sacrificial thermal barrier coatings for core catcher of future sodium cooled fast reactors, Ann. Nucl. Energy 107 (2017) 31–36.
[6] D.R. Clarke, M. Oechsner, N.P. Padture, Thermal-barrier coatings for more efficient gas-turbine engines, MRS Bull. 37 (2012) 891–898.
[7] A. Purwar, D.R. Mahapatra, Design of thermal barrier coating system for scramjet using coupled thermo-structural analysis, Trans. Indian Ceram. Soc. 75 (2016) 242–249.
[8] X. Cao, R. Vassen, D. Stöver, Ceramic materials for thermal barrier coatings, J. Eur. Ceram. Soc. 24 (2004) 1–10.
[9] L. Chen, B. Li, J. Guo, Y. Zhu, J. Feng, High-entropy perovskite $RETa_3O_9$ ceramics for high-temperature environmental/thermal barrier coatings, J. Adv. Ceram. 11 (2022) 556–569.
[10] F. Li, L. Zhou, J.-X. Liu, Y. Liang, G.-J. Zhang, High-entropy pyrochlores with low thermal conductivity for thermal barrier coating materials, J. Adv. Ceram. 8 (2019) 576–582.
[11] D. Liu, B. Shi, L. Geng, Y. Wang, B. Xu, Y. Chen, High-entropy rare-earth zirconate ceramics with low thermal conductivity for advanced thermal-barrier coatings, J. Adv. Ceram. 11 (2022) 961–973.
[12] Z. Tian, S. Lee, G. Chen, Heat transfer in thermoelectric materials and devices, J. Heat Transfer 135 (2013) 061605.
[13] Z. Tian, S. Lee, G. Chen, Comprehensive review of heat transfer in thermoelectric materials and devices, Annu. Rev. Heat Transfer 17 (2014) 425–483.
[14] E.S. Toberer, L.L. Baranowski, C. Dames, Advances in thermal conductivity, Annu. Rev. Mat. Res. 42 (2012) 179–209.
[15] X. Jin, X. Ding, F. Zhan, Q. Gao, R. Wang, X. Yang, X. Lv, Bonding heterogeneity leads to hierarchical and ultralow lattice thermal conductivity in sodium metavanadate, J. Phys. Chem. Lett. 13 (2022) 11160–11168.
[16] Y. Luo, X. Yang, T. Feng, J. Wang, X. Ruan, Vibrational hierarchy leads to dual-phonon transport in low thermal conductivity crystals, Nat. Commun. 11 (2020) 2554.
[17] H.R. Seyf, A. Henry, A method for distinguishing between propagons, diffusions, and locons, J. Appl. Phys. 120 (2016) 025101.
[18] B. Li, F. DeAngelis, G. Chen, A. Henry, The importance of localized modes spectral contribution to thermal conductivity in amorphous polymers, Commun. Phys. 5 (2022) 323.
[19] J. He, C. Yu, S. Lu, S. Shan, Z. Zhang, J. Chen, Complex role of strain engineering of lattice thermal conductivity in hydrogenated graphene-like borophene induced by high-order phonon anharmonicity, Nanotechnology 35 (2023).
[20] H. Zhou, J. Tiwari, T. Feng, Understanding the flat thermal conductivity of $La_2Zr_2O_7$ at ultrahigh temperatures, Phys. Rev. Mater. 8 (2024) 043804.
[21] Y. Ouyang, C. Yu, J. He, P. Jiang, W. Ren, J. Chen, Accurate description of high-order phonon anharmonicity and lattice thermal conductivity from molecular dynamics simulations with machine learning potential, Phys. Rev. B 105 (2022) 115202.
[22] Y. Ouyang, Z. Zhang, C. Yu, J. He, G. Yan, J. Chen, Accuracy of machine learning potential for predictions of multiple-target physical properties, Chin. Phys. Lett. 37 (2020).
[23] Y. Qiu, Z. Jing, H. Liu, H. He, K. Wu, Y. Cheng, B. Xiao, Fast access of the lattice thermal conductivity and phonon quasiparticle spectra of $Mo_2TiC_2T_2$ (T=–O and–F) and Janus Mo_2TiC_2OF MXenes from machine learning potentials, Nanoscale 16 (2024) 7645–7659.
[24] Y. Ouyang, C. Yu, G. Yan, J. Chen, Machine learning approach for the prediction and optimization of thermal transport properties, Front. Phys. 16 (2021).
[25] Y. Hao, Y. Zuo, J. Zheng, W. Hou, H. Gu, X. Wang, X. Li, J. Sun, X. Ding, Z. Gao, Machine learning for predicting ultralow thermal conductivity and high ZT in complex thermoelectric materials, ACS Appl. Mater. Interfaces 16 (2024) 47866–47878.
[26] A. Pazhedath, L. Bastonero, N. Marzari, M. Simoncelli, First-principles characterization of thermal conductivity in $LaPO_4$-based alloys, Phys. Rev. Appl 22 (2024) 024064.
[27] M. Simoncelli, N. Marzari, F. Mauri, Wigner formulation of thermal transport in solids, Phys. Rev. X 12 (2022) 041011.
[28] B. Mortazavi, E.V. Podryabinkin, I.S. Novikov, S. Roche, T. Rabczuk, X. Zhuang, A. V. Shapeev, Efficient machine-learning based interatomic potentialsfor exploring thermal conductivity in two-dimensional materials, J. Phys.: Mater. 3 (2020) 02LT02.
[29] I.S. Novikov, K. Gubaev, E.V. Podryabinkin, A.V. Shapeev, The MLIP package: moment tensor potentials with MPI and active learning, Mach. Learn.: Sci. Technol. 2 (2020) 025002.
[30] J. Hafner, Ab-initio simulations of materials using VASP: Density-functional theory and beyond, J. Comput. Chem. 29 (2008) 2044–2078.
[31] G. Kresse, J. Furthmüller, Efficiency of ab-initio total energy calculations for metals and semiconductors using a plane-wave basis set, Comput. Mater. Sci. 6 (1996) 15–50.
[32] G. Kresse, D. Joubert, From ultrasoft pseudopotentials to the projector augmented-wave method, Phys. Rev. B 59 (1999) 1758.
[33] P.E. Blöchl, Projector augmented-wave method, Phys. Rev. B 50 (1994) 17953.
[34] J.P. Perdew, K. Burke, M. Ernzerhof, Generalized gradient approximation made simple, Phys. Rev. Lett. 77 (1996) 3865.
[35] G.J. Martyna, M.L. Klein, M. Tuckerman, Nosé–Hoover chains: The canonical ensemble via continuous dynamics, J. Chem. Phys. 97 (1992) 2635–2643.
[36] K. Momma, F. Izumi, VESTA: a three-dimensional visualization system for electronic and structural analysis, Appl. Crystallograp. 41 (2008) 653–658.
[37] B. Mortazavi, X. Zhuang, T. Rabczuk, A.V. Shapeev, Atomistic modeling of the mechanical properties: the rise of machine learning interatomic potentials, Mater. Horizons 10 (2023) 1956–1968.
[38] A. Carreras, A. Togo, I. Tanaka, DynaPhoPy: A code for extracting phonon quasiparticles from molecular dynamics simulations, Comput. Phys. Commun. 221 (2017) 221–234.
[39] A. Togo, I. Tanaka, First principles phonon calculations in materials science, Scr. Mater. 108 (2015) 1–5.
[40] A.P. Thompson, H.M. Aktulga, R. Berger, D.S. Bolintineanu, W.M. Brown, P. S. Crozier, P.J. In't Veld, A. Kohlmeyer, S.G. Moore, T.D. Nguyen, LAMMPS-a flexible simulation tool for particle-based materials modeling at the atomic, meso, and continuum scales, Comput. Phys. Commun. 271 (2022) 108171.
[41] A. Togo, First-principles phonon calculations with phonopy and phono3py, J. Phys. Soc. Jpn. 92 (2023) 012001.

[42] A. Togo, L. Chaput, T. Tadano, I. Tanaka, Implementation strategies in phonopy and phono3py, J. Phys. Condens. Matter 35 (2023) 353001.
[43] Z. Han, X. Yang, W. Li, T. Feng, X. Ruan, FourPhonon: An extension module to ShengBTE for computing four-phonon scattering rates and thermal conductivity, Comput. Phys. Commun. 270 (2022) 108179.
[44] W. Li, J. Carrete, N.A. Katcho, N. Mingo, ShengBTE: A solver of the Boltzmann transport equation for phonons, Comput. Phys. Commun. 185 (2014) 1747–1758.
[45] J.A. Thomas, J.E. Turney, R.M. Iutzi, C.H. Amon, A.J. McGaughey, Predicting phonon dispersion relations and lifetimes from the spectral energy density, Phys. Rev. B—Conden. Matter Mater. Phys. 81 (2010) 081411.
[46] Z. Tong, Y. Zhang, A. Pecchia, C. Yam, L. Zhou, T. Dumitrică, T. Frauenheim, Predicting the lattice thermal conductivity in nitride perovskite $LaWN_3$ from ab initio lattice dynamics, Adv. Sci. 10 (2023) 2205934.
[47] D.-S. Tang, L.-M. Zhang, Phonon modes and topological phonon properties in $(GaN)_x/(AlN)_x$ and $(AlGaN)_x/(GaN)_x$ superlattices, Phys. Scr. 98 (2023) 085934.
[48] H. Dong, Z. Li, B. Sun, Y. Zhou, L. Liu, J.-Y. Yang, Thermal transport in disordered wurtzite ScAlN alloys using machine learning interatomic potentials, Mater. Today Commun. 39 (2024) 109213.
[49] M. Puligheddu, Y. Xia, M. Chan, G. Galli, Computational prediction of lattice thermal conductivity: A comparison of molecular dynamics and Boltzmann transport approaches, Phys. Rev. Mater. 3 (2019) 085401.
[50] H. Chen, Y. Gao, Y. Liu, H. Luo, Coprecipitation synthesis and thermal conductivity of $La_2Zr_2O_7$, J. Alloys Compd. 480 (2009) 843–848.
[51] Y. Wang, F. Yang, P. Xiao, Glass-like thermal conductivities in $(La_{1-x1}Y_{x1})_2(Zr_{1-x2}Y_{x2})_2O_{7-x2}$ ($x = x_1 + x_2$, $0 \leqslant x \leqslant 1.0$) solid solutions, Acta Materialia 60 (2012) 7024–7033.
[52] J. Xiang, S. Chen, J. Huang, H. Zhang, X. Zhao, Phase structure and thermophysical properties of co-doped La_2Zr_2O7 ceramics for thermal barrier coatings, Ceram. Int. 38 (2012) 3607–3612.
[53] Y. Zhang, M. Xie, F. Zhou, X. Cui, X. Lei, X. Song, S. An, Low thermal conductivity in $La_2Zr_2O_7$ pyrochlore with A-site partially substituted with equimolar Yb_2O_3 and Er_2O_3, Ceram. Int. 40 (2014) 9151–9157.
[54] J. Feng, C. Wan, B. Xiao, R. Zhou, W. Pan, D.R. Clarke, Calculation of the thermal conductivity of L2SrAl2O7 (L= La, Nd, Sm, Eu, Gd, Dy), Phys. Rev. B—Conden. Matter Mater. Phys. 84 (2011) 024302.
[55] H. Dong, X. Chen, J. Li, P. Jia, Y. Shuang, Q. Sun, W. Ma, Preparation and Thermal Properties of $LaPO_4$ Ceramics, IOP Conference Series: Materials Science and Engineering, (2019) IOP Publishing, pp. 012079.
[56] A. Du, C. Wan, Z. Qu, W. Pan, Thermal conductivity of monazite-type $REPO_4$ (RE= La, Ce, Nd, Sm, Eu, Gd), J. Am. Ceram. Soc. 92 (2009) 2687–2692.
[57] A. Du, C. Wan, Z. Qu, R. Wu, W. Pan, Effects of texture on the thermal conductivity of the $LaPO_4$ monazite, J. Am. Ceram. Soc. 93 (2010) 2822–2827.
[58] A.B. Du, R.F. Wu, Z.X. Qu, C.L. Wan, W. Pan, Thermal conductivities of $LaPO_4$/Al_2O_3 composites fabricated by SPS, Key Eng. Mater. 434 (2010) 123–125.
[59] E.S. Toberer, A. Zevalkink, G.J. Snyder, Phonon engineering through crystal chemistry, J. Mater. Chem. 21 (2011) 15843–15852.